Land Surface Temperature Variation and Major Factors in Beijing, China

Rongbo Xiao, Qihao Weng, Zhiyun Ouyang, Weifeng Li, Erich W. Schienke, and Zhaoming Zhang

Abstract

Land surface temperature (LST) is a significant parameter in urban environmental analysis. Current research mainly focuses on the impact of land-use and land-cover (LULC) on LST. Seldom has research examined LST variations based on the integration of biophysical and demographic variables, especially for a rapidly developing city such as Beijing, China. This study combines the techniques of remote sensing and geographic information system (GIS) to detect the spatial variation of LST and determine its quantitative relationship with several biophysical and demographic variables based on statistical modeling for the central area of Beijing. LST and LULC data were retrieved from a Landsat Thematic Mapper (TM) image. Building heights were delimited from the shadows identified on a panchromatic SPOT image. The integration of LULC and census data was further applied to retrieve grid-based population density. Results indicate that the LST pattern was non-symmetrical and non-concentric with high temperature zones clustered towards the south of the central axis and within the fourth ring road. The percentage of forest, farmland, and water per grid cell were found to be most significant factors, which can explain 71.3 percent of LST variance. Principal component regression analysis shows that LST was positively correlated with the percentage of low density built-up, high density built-up, extremely-high buildings, low buildings per grid cell, and population density, but was negatively correlated with the percentage of forest, farmland, and water bodies per grid cell. The findings of this study can be applied as the theoretical basis for improving urban planning for mitigating the effects of urban heat islands.

Introduction

Land surface temperature (LST) is an important parameter in study of urban thermal environment and behavior. LST modulates the air temperature of the lower layer of urban atmosphere, and is a primary factor in determining surface radiation and energy exchange, the internal climate of buildings, and human comfort in the cities (Voogt and Oke, 1998). The physical properties of various types of urban surfaces, their color, the sky view factor, street geometry, traffic loads, and anthropogenic activities are important factors that determine LSTs in the urban environments (Chudnovsky *et al.*, 2004). The LST of urban surfaces correspond closely to the distribution of land-use and land-cover (LULC) characteristics (Lo *et al.*, 1997; Weng, 2001 and 2003; Weng *et al.*, 2004). Each component surface in urban landscapes (e.g., lawn, parking lot, road, building, cemetery, and garden) exhibits unique radiative, thermal, moisture, and aerodynamic properties and relates to their surrounding site environment (Oke, 1982). The myriad of these component surfaces and the spatial complexity when they are mosaicked create a limitless array of energy balance and microclimate systems (Oke, 1982). To study urban LSTs, some sophisticated numerical and physical models have been developed. These include energy balance models (Oke *et al.*, 1999; Tong *et al.*, 2005), laboratory models (Cendese and Monti, 2003), three-dimensional simulations (Saitoh *et al.*, 1996), Gaussian models (Streutker, 2003), and other numerical simulations (Yang *et al.*, 2003). Among these models and simulations, energy balance models are by far the main methods, but statistical analysis may play an important role in linking LST to related factors, especially at larger scales (Bottyán and Unger, 2003). Previous studies have focused primarily on biophysical and meteorological factors, such as built-up area and height (Bottyán and Unger, 2003), urban and street geometry (Eliasson, 1996), LULC (Dousset and Gourmelon, 2003), and vegetation (Weng *et al.*, 2004). A less number of studies, however, have examined how population distribution influences urban heat island (UHI) intensity, although it is apparently an indicator of anthropogenic heat emission (Fan and Sailor, 2005) and the intensity of human activities (Elvidge *et al.*, 1997).

Little research effort has been made to study the intra-urban variations of LST and their related biophysical and socioeconomic variables within a city. The combination of biophysical and socioeconomic data for urban studies has been hampered by the spatial unit problem, because the relevant spatial units for biophysical processes are different from the spatial units for population and other

Rongbo Xiao is with the National State Key Lab of Urban and Regional Ecology, Research Center for Eco-Environmental Sciences, Chinese Academy of Sciences, Beijing, China (ecoxiaorb@163.com).

Zhiyun Ouyang and Weifeng Li are with the National State Key Lab of Urban and Regional Ecology, Research Center for Eco-Environmental Sciences, Chinese Academy of Sciences, Beijing, 100085 China.

Qihao Weng is with the Department of Geography, Geology, and Anthropology, Indiana State University, Terre Haute, IN.

Erich W. Schienke is with the Department of Science and Technology Studies, Rensselaer Polytechnic Institute, Troy, NY.

Zhaoming Zhang is with the China Remote Sensing Satellite Ground Station, Chinese Academy of Sciences, Beijing, China.

Photogrammetric Engineering & Remote Sensing
Vol. 74, No. 4, April 2008, pp. 451–461.

0099-1112/08/7404–0451/$3.00/0

socioeconomic data (Yuan *et al.*, 1997). Recent significant advances in the data and technological integration between remote sensing and GIS suggest that the integration is a powerful and effective tool in urban studies. Remote sensing from airborne or satellite platforms cannot only provide thermal infrared data, but also LULC, building height, and other urban biophysical variables. GIS technology provides powerful capability for entering, analyzing, and displaying digital data from various sources and formats. In order to gain a deeper insight into urban thermal behavior and climate, more research is needed to explore LST's relationship with various biophysical and socioeconomic variables using an integrated remote sensing and GIS approach. Moreover, this integration may help serve to bridge the gap between scientific studies of urban climate and their applications in planning and environmental management.

Beijing, the capital of China, has experienced a rapid urban expansion over the past two decades. Accelerated urban development and lack of appropriate planning measures have created serious impacts on its thermal environment. It is found that air temperature UHI effect in Beijing became more evident, where average daily air temperature in the urban area was 4.6°C higher than that in the suburban area (Song and Zhang, 2003). Existing UHI studies in Beijing have been focused primarily on the temporal dynamics of air temperatures. Further analysis of the spatial patterns of its LST and the contributing factors is urgently needed. In this study, we combine remote sensing and GIS to analyze the spatial pattern of LST and explore the factors that have contributed to the LST variations. Considering the study area's unique geographical setting and data availability, this study identifies potential explanatory variables from LULC, building heights distribution, and population density. The information on LULC, LST, and building heights will be extracted from remote sensing data. Grid based population density will then be computed by integrating LULC and census population. Statistical analyses will explore how the LST variation to be a function of the biophysical and demographic variables. This analysis would provide useful information for designing measures to effectively mitigate the UHI effects and thus improve the thermal environment of Beijing.

Study Area

Beijing, one of the largest cities in the world, covers approximately 16,800 km^2 with a population of 13 million people. It is the political, cultural, and communication center of China, and has a history of more than 3,000 years as a city and more than 800 years as a capital city. It has been selected as the site of 2008 Summer Olympic Games. Over the past two decades, Beijing has undergone significant LULC changes characterized by accelerated urbanization. The development pattern is typically a concentric expansion, which forms an obvious ring-shaped pattern from the inner center to the outskirts. Our study area focuses within the fifth-ring road, where the majority of built-up takes place. This area occupies 666.7 km^2 comprised by nine counties and 120 townships. Beijing resides on a plain, with the elevation at approximately 100 m above mean sea level. It is located in the temperate climatic zone, and has a mean annual temperature of 12°C, and an average annual precipitation of 640 mm. The study area was divided into 1000 m × 1000 m grids (Figure 1) in order to compute grid-based population density and to conduct data integration for statistical analysis.

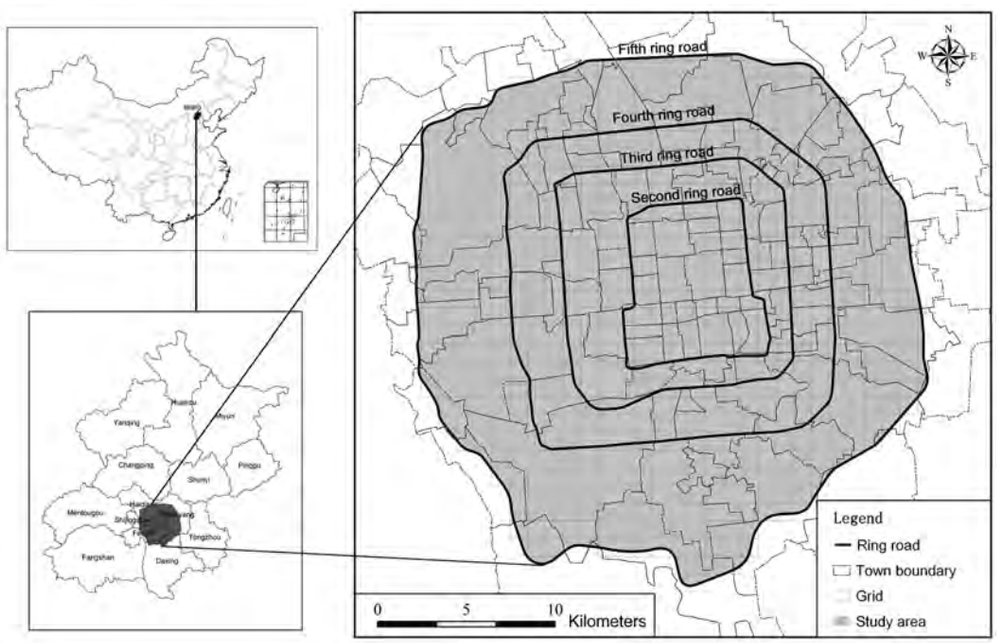

Figure 1. Location of the study area.

Data and Methods

Data Used

Five primary data sources were employed in this study: (a) Beijing 2000 census data by township, (b) a Landsat-5 TM scene acquired on 31 August 2001, which was close to the completion date of 2000 China census and was used to extract LST and LULC information, (c) a Panchromatic SPOT image acquired on 13 November 2000, which was used to extract building heights, (d) meteorological data from weather stations on 31 August 2001 used as the input parameters to retrieve LST, and (e) 1:10 000 topography and road maps obtained from Beijing Institute of Surveying and Mapping. All data were geometrically referenced to the 1:10 000 topographic maps to facilitate the analysis.

LULC Information Extraction

A supervised classification with the maximum likelihood algorithm was conducted to classify the Landsat TM image (using all reflected bands, 1 through 5, and 7). Six LULC categories were identified, including high-density built-up, low-density built-up, forest, farmland, water, and exposed land. High-density built-up consists of approximately 80 to 100 percent construction materials, which are typically old commercial, residential, and industrial buildings as well as large transportation facilities. Low-density built-up consists of 50 to 80 percent construction materials, which have mostly been reconstructed in recent years, and frequently contains some small open space. Then, a road map, created by Beijing Institute of Surveying and Mapping, was combined with the LULC results in order to obtain the seventh LULC type: road. Accuracy of the classification map was verified by field checking or by comparing with existing LULC maps that have been field checked. The overall accuracy of the LULC map was determined to be 83.86 percent and Kappa index of 85.52 (Table 1).

Calculation of NDVI

Normalized Vegetation Index (NDVI) was calculated from the TM image using the following formula:

$$NDVI = \frac{\rho(band\ 4) - \rho(band\ 3)}{\rho(band\ 4) + \rho(band\ 3)} \quad (1)$$

where ρ is band reflectivity. $NDVI_{TOA}$ and $NDVI_{surf}$ were obtained by using values from at-sensor and at-surface reflectivity, respectively. The latter is more accurate due to atmospheric correction, and thus was used in this study.

The at-surface reflectivity was calculated with the following equation (Chavez, 1996):

$$\rho_{\text{surf}} = \frac{\pi(L_{sat} - L_p)d^2}{E_0 \cos\theta_z T_z} \quad (2)$$

where L_{sat} is the at-sensor radiance, T_z is the atmospheric transmissivity between the sun and the surface, θ_z is the zenithal solar angle, E_0 is the spectral solar irradiance on the top of the atmosphere, d is the Earth-Sun distance, and L_p is the radiance with the atmospheric components (molecules and aerosols) that can be obtained according to the following equation:

$$L_p = L_{\min} - L_{1\%} \quad (3)$$

where $L_{\min}$ is the radiance that corresponds to a digital count value for which the sum of all the pixels with digital counts lower or equal to this value is equal to 0.01 percent if all the pixels from the image is considered. The term $L_{1\%}$ is given by:

$$L_{1\%} = \frac{0.01\cos\theta_z T_z E_0}{\pi d^2} \quad (4)$$

with values for T_z equal to 0.85 and 0.91 for bands TM3 and TM4, respectively (Chavez, 1996).

Derivation of LST

Landsat TM thermal infrared data (band 6) with the wavelength range of 11.45 to 12.50 μm and a nominal ground resolution of 120 m $\times$ 120 m has been proved effective to obtain LST information. To retrieve LST from one thermal band, some atmospheric parameters are needed to be considered, usually by a complicated procedure of radio-sounding. Many previous studies with Landsat TM thermal data concentrated on computing and applying brightness temperatures only. In this study, a mono-window algorithm was applied to obtain LSTs to avoid the radio-sounding procedure (Qin *et al.*, 2001):

$$T_s = \frac{1}{C}[a(1 - C - D) + (b(1 - C - D) + C + D)T_{sensor} - DT_\alpha] \quad (5)$$

with $C = \varepsilon\tau$, $D = (1 - \tau)[1 + (1 - \varepsilon)\tau]$, $\alpha = -67.355351$, and $b = 0.458606$, where ε is land surface emissivity (LSE), τ is the total atmospheric transmissivity, T_{sensor} is the at-sensor

TABLE 1. ERROR MATRIX AND ACCURACY ASSESSMENT RESULT OF THE LULC MAP

	Reference Data						
Classified Data	Road	Exposed Land	Forest	Water	Low-density Built-up	High-density Built-up	Farmland
Road	56	0	0	0	0	0	0
Exposed land	0	16	0	0	0	1	5
Forest	0	0	37	0	0	0	1
Water	0	1	0	10	0	2	0
Low-density built-up	0	1	4	1	125	9	3
High-density built-up	0	4	0	1	5	80	0
Farmland	0	0	2	0	1	1	11
Total	56	22	43	12	131	93	20
Producers Accuracy %	100	72.73	86.05	83.33	95.42	86.02	55.00
Users Accuracy %	100	72.73	97.37	76.92	87.41	88.89	73.33
Kappa	1	0.7104	0.9703	0.7616	0.8071	0.8525	0.7184

Overall Classification Accuracy = 88.86; Overall Kappa Statistics = 0.8552.

brightness temperature, and T_α represents the mean atmospheric temperature given by:

$$T_\alpha = 16.0110 + 0.92621T_0 \quad (6)$$

with T_0 being the near-surface air temperature. Qin *et al.* (2001) also estimated the atmospheric transmissivity from w, the atmospheric water vapor content, for the range 0.4 to 1.6 g/cm^2, according to the following equations:

$$\tau = 0.974290 - 0.08007w \text{ (high } T_0\text{), and} \quad (7)$$

$$\tau = 0.982007 - 0.09611w \text{ (low } T_0\text{).} \quad (8)$$

Both T_0 and w were obtained from local meteorological stations. LSE is obtained by using the NDVI thresholds method (Sobrino *et al.* 2004):

$$\varepsilon = \varepsilon_{soil}, \text{ when NDVI} < 0.2, \quad (9)$$

$$\varepsilon = \varepsilon_{veg}, \text{ when NDVI} > 0.5, \text{ and} \quad (10)$$

$$\varepsilon = \varepsilon_{veg}P_v + \varepsilon_{soil}(1 - P_v) + d\varepsilon, \text{ when } 0.2 \geq \text{NDVI} \leq 0.5, \quad (11)$$

where ε_{soil} is the soil emissivity, ε_{veg} is the vegetation emissivity, and $d\varepsilon$ includes the effects of the geometry of natural surfaces and the internal reflections. Because most of the study area is a plain surface, this term is negligible. P_v is the proportion of vegetation that can be computed by the following formula (Carlson and Ripley, 1997):

$$P_v = \left[\frac{NDVI - NDVI_{\min}}{NDVI_{\max} - NDVI_{\min}}\right]^2 \quad (12)$$

where $NDVI_{\max} = 0.5$, and $NDVI_{\min} = 0.2$. Soil and vegetation emissivities were estimated to be 0.97 and 0.99, respectively (Sobrino et al., 2004).

Computation of Building Heights

Building heights were calculated from shadows that were identified on a panchromatic SPOT image (Cheng and Thiel, 1995). The height h is calculated as follows:

$$h = \tan\beta \times S \quad (13)$$

where β is sun elevation, S is the shadow length in the converse direction of sun azimuth ω in the geometric corrected image, and β, ω can be retrieved from the SPOT header file.

The shadow length S_N in the north direction was calculated as per pixel values. The shadow length S in the converse direction of sun azimuth ω can be calculated with the following formula:

$$S = 10S_N/\sin(\omega - 90°) \quad (14)$$

where S_N is the pixel number in the north direction, which can be obtained from the SPOT image, and ω is sun azimuth. In this study, we obtained $\beta = 32.3959°$, and $\omega = 173.593°$, then $h = 6.4 * S_N$. All buildings were categorized into three levels according to S_N values, i.e., extremely-high buildings (>38.4 m), medium-high buildings (25.6 to 38.4 m), and low buildings (12.8 to 25.6 m). Buildings lower than 12.8 m were not detectable from the satellite image.

Calculation of Grid-based Population Density

Previous research have primarily adopted a census polygon overlay method to analyze the relationship between population and LST (Elvidge *et al.*, 1997). However, the value in a particular enumeration district (ED) implies the aggregate value of the entire district without any internal variation. Besides implying the notion of evenly distributed populations, census boundaries may or may not coincide with actual ecological landscape patterns (Moon and Farmer, 2001). In this study, LULC classification derived from the TM image was applied to compute per-pixel based population (Yuan *et al.*, 1997). This method assumes that population distribution is related to LULC (Flowerdew and Green, 1989). The regression models for population estimation are additive linear models of the following form:

$$P_i = \sum_{j=1}^{k}(\eta_j r_{ij} + \varepsilon_i) \quad (15)$$

where P_i is the total population count for i^{th} ED, η_j is the average population density for the j^{th} LULC type, and independent variables r_{ij} are the total areas for the j^{th} LULC type within the i^{th} ED.

Because population density distribution is not explained solely by LULC, it is necessary to refine η_j as follows:

$$\eta_{ij} = \frac{P_i}{y_i} \times \eta_i \quad (16)$$

where η_{ij} is the refined population density for the j^{th} LULC within the i^{th} ED, and y_i is predicted total population of the i^{th} ED. The i^{th} grid population density is computed as follows:

$$Q_i = \sum_{j=1}^{k}(\eta_{ij} A_{ij}) \quad (17)$$

where Q_i is the total population count for i^{th} grid, and A_{ij} are the total areas for the j^{th} LULC type within the i^{th} grid.

Statistical Analysis of the Relationship Between LST and Related Factors

In order to analyze the relationship between LST and related factors, we identified the following explanatory variables, including: population density (PD), the percentages of high-density built-up (HD), low-density built-up (LD), forest (FO), farmland (FA), water (WA), expose land (EL), extremely-high buildings (EH), medium-high buildings (MH), and low buildings (LH), and computed their values per grid. At first, multiple stepwise regressions (MSR) were applied to obtain s independent variables with statistical significances ($P < 0.001$), and to examine whether the s independent variables had multicollinearity. If there was a multicollineatity, principal component regressions (PCR) would then be applied consequently, which is the method of combining linear regression with principal component analysis (PCA). PCA can transform a set of correlated variables into a set of uncorrelated principal components (Montgomery and Peck, 1992). MSR and PCR were carried out with SPSS 11.0 (Liu *et al.*, 2003).

Results

Spatial Characteristics of LST and Land-cover Parameters

Across the entire study area, LST values increased from the outskirts towards the inner urban areas, which ranged from 16.4° to 40.5°C, with a mean of 26.6°C and a standard deviation of 2.7°. LST patterns were found to be non-symmetrical and non-concentric, with high temperature zones clustered towards the south of the central axis and within the fourth ring road (Figure 2). In contrast, the value of NDVI varied from −0.655 to 0.638, with a mean value of 0.002 and a standard deviation of 0.164. Figure 3 shows that low NDVI values were detected at the center of the study area, corresponding to the built-up areas (such as buildings, roads, etc.). High NDVI values were discovered largely in the surrounding areas, corresponding to green vegetation. The spatial pattern of NDVI appeared to be concentric. High NDVI

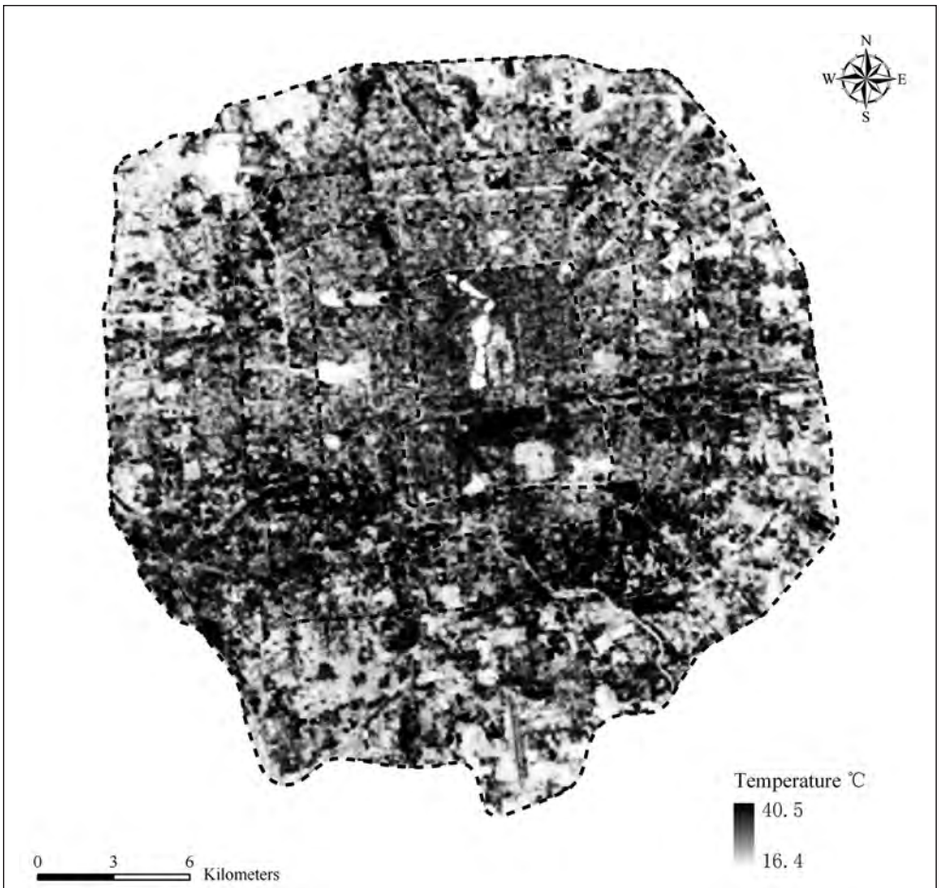

Figure 2. Spatial distribution of land surface temperature.

values formed a belt between the fourth and fifth ring roads, and was scattered within the third ring road, consistent with the distribution of parks and recreation sites.

Plate 1 displays LULC distribution in Beijing. Low-density and high-density built-up were the dominant types, which occupied about 64.85 percent of the total area (432.36 km^2). The radial roads, ring roads, and smaller artery roads converged to become the transportation network, which accounted for a total area of 97.92 km^2. Forest shared 11.01 percent in area (73.44 km^2), mainly seen between the fourth and the fifth ring roads, as well as in some large parks. Exposed land were those lands either set aside for future urban development, or was extremely difficult for current use. These lands were mainly located beyond the fourth ring road. Farmland and water were relatively small, together comprising only 3.49 percent of the area (Table 2).

LST and NDVI values by LULC type were computed to understand further how LST interacted with land cover parameters. The highest LST was found in high-density built-up areas (28.61°C), followed by exposed land (26.94°C), roads (26.75°C), low-density built-up (26.60°C). Lowest temperatures were detected with water bodies (19.97°C), farmland (21.96°C), and forest (22.94°C). The highest NDVI was found in farmland (0.36), followed by forest (0.26), low-density built-up (−0.01), road (−0.03), high-density built-up (−0.11), and water (−0.12) (Table 2). This implies that urban development has brought up LST by replacing natural vegetation with non-evaporating and non-transpiring surfaces such as stone, metal, and concrete (Lo *et al.*, 1997; Weng, 2001).

Characteristics of Building and Population Density Distributions

The distribution of building heights within the city was delineated based on the shadows on a panchromatic SPOT image. Results show that there were 69,624 low buildings, occupying a total area of 51.31 km^2. These buildings were scattered throughout the study area. A total of 15,778 medium to high buildings were discovered (12.47 km^2 in area), while 4,068 extremely-high buildings were measured to account for only 5.71 km^2. Both medium and extremely high buildings were primarily located close to the main roads, some residential districts, and within business districts (Plate 2).

Census population density value of EDs ranged from 196 to 39,874 persons/km^2, with a mean value of 7,448 persons/km^2 (Figure 4). Strong correlation was found between census population density and LULC (R^2 = 0.773). Using LULC for population estimation, the rasterized population density ranged from 286 to 34,408 persons/km^2, with a mean value of 10,532 persons/km^2 (Figure 5). Comparing the map of the census population distribution and LULC-based population density map, it is clear that the latter can reveal more spatial variations with regard to LST distribution.

Results of Statistical Analysis

Table 3 shows the result of stepwise correlation analysis. LST was found significantly correlated with eight variables, including FO, FA, WA, LD, HD, EH, PO, and LH (R^2 = 0.811). Forest, farmland, and water were the three strongest factors

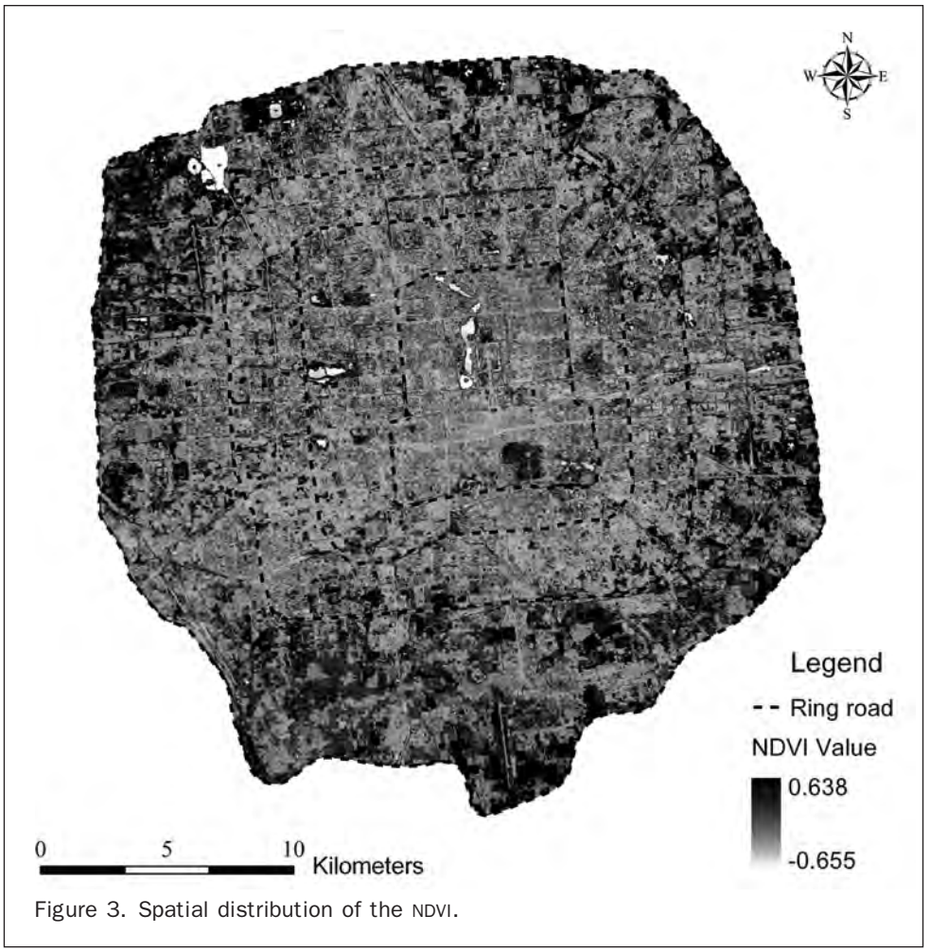

Figure 3. Spatial distribution of the NDVI.

with R^2 of 0.713, which means these three variables were able to explain 71.3 percent of the relationship. The ratios of exposed land, roads, and medium-height buildings by grid did not enter the regression model. Based on the fact that ninth eigenvalue is close to 0 (0.007) and the condition index is more than 15 (27.425) (Table 4), there was a significant amount of multicollinearity among the eight variables. The presence of such strong multicollinearity makes MSR models less useful and inappropriate.

Principal component analysis shows the first four principal components (PCs) can explain 85.276 percent of the total variation in LST (Table 5). From the factor loading matrix, a mathematical expression between PCs and the primal eight variables can be established:

$$PC = Ax, \tag{18}$$

where PC is the first four principal components matrix, A is first four principal components loading matrix, and x is the matrix consisted of FO, FA, WA, LD, HD, EH, PO, and LH (Table 5).

The standardized principal component regression equation was performed to evaluate the relationship between LST and the first four PCs, and obtained the following result:

$$\text{LST} = 0.329\text{PC}_1 - 0.776\text{PC}_2 + 0.216\text{PC}_3 + 0.086\text{PC}_4 \tag{19}$$

($R^2 = 0.764$; significance = 0.001)

Applying Equation 18 to Equation 19, the final model of LST can be presented as follows:

$$\text{LST} = 25.525 - 4.283\text{FO} - 5.847\text{FA} - 8.272\text{WA} + 6.019\text{LD} + 0.615\text{HD} + 2.908\text{HB} + 17.315\text{PO} + 3.440\text{LH}, \tag{20}$$

where FO, FA, WA, LD, HD, EH, LH, and PO are the ratios of forest, farmland, water, low-density built-up, high-density built-up, extremely-high buildings, low buildings by grid, population density, respectively. It is concluded that LST was positively correlated to the ratios of low-density built-up, high-density built-up, extremely-high buildings, low buildings by grid, and population density, but was negatively correlated with the ratios of forest, farmland, and water bodies by grid.

Discussion and Conclusions

This study has investigated the spatial distribution of LST and its quantitative relationships with biophysical and demographic parameters in Beijing. The results indicate that the spatial pattern of LST was non-symmetrical and non-concentric with high temperature zones clustered towards the south of the central axis and within the fourth ring road. The ratios of forest, farmland, and water were found to be most significant factors in explaining the LST variation. Principal component regression analysis further shows that LST was positively correlated with the ratios of low-density

Plate 1. Land-use and land-cover map.

built-up, high-density built-up, extremely-high buildings, low buildings, and population density, while negatively correlated with the ratios of forest, farmland, and water bodies.

Landsat TM thermal infrared data is suitable to derive meso-scale temperatures in urban areas, but many studies mainly apply brightness temperatures or original DN values (Aniello *et al.*, 1995). In this study, we applied a mono-window algorithm to retrieve LST, which was developed by Qin *et al.* (2001) and tested by other researchers (Sobrino *et al.*, 2004). This approach can provide more accurate LST measurements and is suitable for a better urban analysis. It is worthy to note that LST is different from air temperature, although several studies have found good correlations between them (Ben-Dor and Saaroni, 1997). It should be pointed out that this study was limited by Landsat-5 TM data with low temporal resolution, which passed over in Beijing at about 10:40 local time. Future research of LST will benefit from higher spectral, temporal, and spatial resolution of new remote sensing instruments such as ASTER. Further data integration is required to study daily and seasonal fluctuations in LST, where remotely sensed imagery can be combined with temperature measurements of local meteorological stations and *in situ* measurements.

This study indicates, as expected, that high- and low-density built-up and road areas possessed higher LST, while

TABLE 2. TOTAL AREA, LAND SURFACE TEMPERATURE, AND NDVI BY LAND-USE/COVER TYPE

	Area		NDVI		Land Surface Temperature	
LULC TYPE	km^2	%	Mean	Std. Dev.	Mean	Std. Dev.
High-density built-up	138.5	20.77	−0.11	0.15	28.61	1.76
Low-density built-up	293.85	44.07	−0.01	0.12	26.6	2.00
Road	97.92	14.69	−0.03	0.14	26.75	2.13
Forest	73.44	11.01	0.26	0.13	22.94	1.71
Farmland	13.02	1.95	0.36	0.11	21.96	1.53
Water	10.28	1.54	−0.12	0.21	19.97	2.01
Expose land	39.7	5.95	0.02	0.15	26.94	2.35

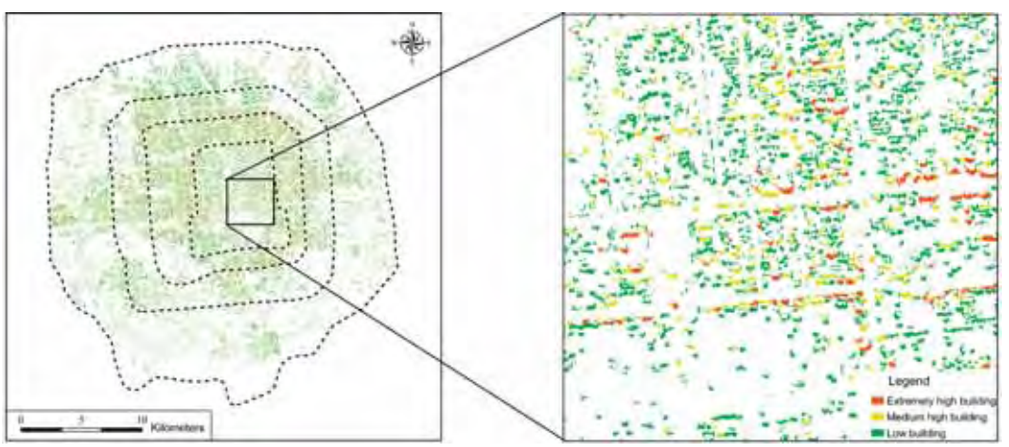

Plate 2. Building height distribution.

forest, farmland, and water bodies yielded much lower LST. This finding suggests that urban/built-up uses play an important role in LST variations, which confirms the conclusions made by previous studies (Dousset and Gourmelon, 2003; Weng and Yang, 2004). Roads in this study did not exhibit the highest temperature, which is inconsistent with some other studies, where high thermal signatures on roads were usually detected as a result of construction materials, heat emissions from combustion engines, and polluted air (Chudnovsky *et al.*, 2004). This may be due to the fact that there are many plants and green spaces on the sides of most roads in Beijing. It may also have something to do with the differences in the thermal properties between roads and roofs. Temperatures of roofs were likely to be warmer than roads, especially in the morning, since roofs would heat up more quickly due to its low thermal admittance. In addition,

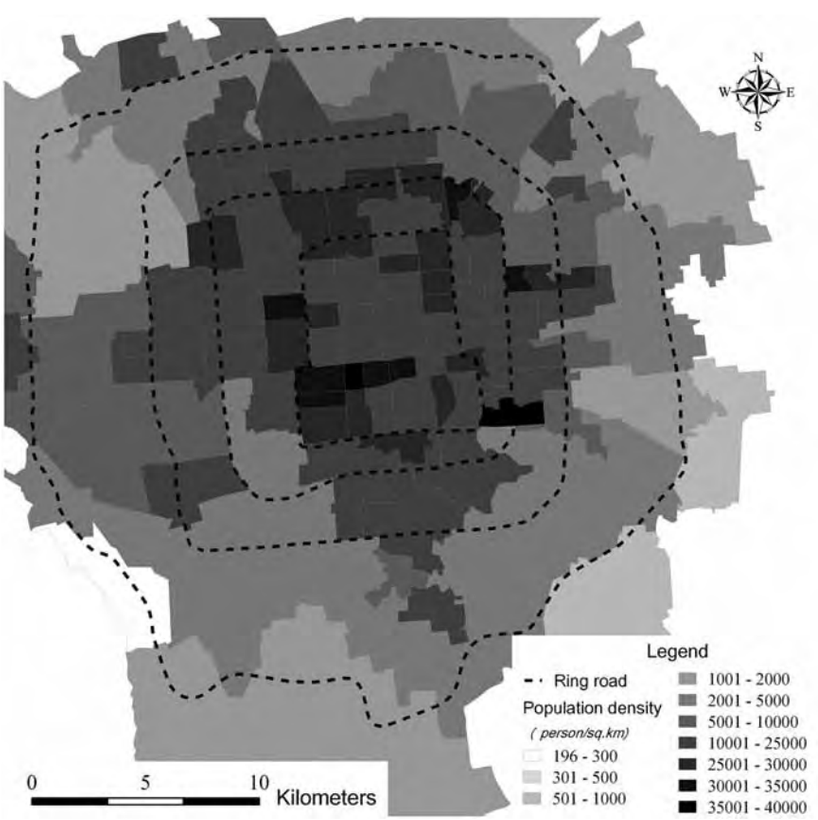

Figure 4. Spatial distribution of population density of census districts.

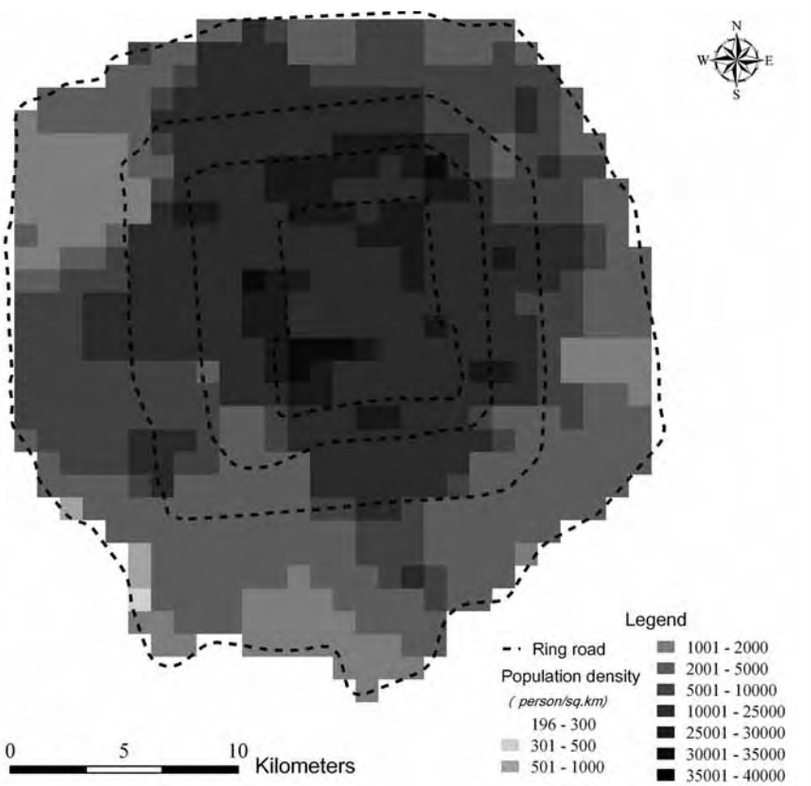

Figure 5. Spatial distribution of grid-based population density.

forest temperature was detected to be higher than farmland, a finding that is different from a similar study in Guangzhou, China (Weng and Yang, 2004). The main reason is possibly that forest in Beijing is distributed around dense urban uses and is strongly influenced by the surrounding areas, while farmland is located mainly in the suburbs where building density is substantially lower.

The stepwise regression model entered eight variables, but the ratios of forest, farmland, and water were the three most influential variables. Apparently, these natural covers were important factors in controlling LST variation. Vegetation types have distinct thermal properties of radiating surfaces from urban/built-up uses, and consume much energy by evapotranspiration (Weng *et al.*, 2004). The cooling function of water was similar to vegetation. In addition, the ratios of extremely high buildings and low buildings were found to have a significant impact on the LST. High buildings can change urban canyon geometry and thermal characteristics vertically, leading to the increase in absorption of shortwave radiation and the decrease in outgoing longwave radiation, and hindering the loss of sensible heat (Bottyán and Unger, 2003; Voogt and Oke, 1998). An interesting finding in this study is that the ratios of roads, exposed land, and medium-high buildings did not enter the regression model. This is likely due to their close correlations with above-mentioned eight variables.

TABLE 3. STEPWISE CORRELATION COEFFICIENTS AND THEIR SIGNIFICANCE LEVELS

Parameters Entered	R	R^2	Significance Level
FO	0.575	0.331	0.001
FO, FA	0.756	0.572	0.001
FO, FA, WA	0.845	0.713	0.001
FO, FA, WA, LD	0.883	0.780	0.001
FO, FA, WA, LD, HD	0.887	0.787	0.001
FO, FA, WA, LD, HD, EH	0.891	0.794	0.001
FO, FA, WA, LD, HD, EH, PO	0.897	0.804	0.001
FO, FA, WA, LD, HD, EH, PO, LH	0.901	0.811	0.001

Note: FO, FA, WA, LD, HD, EH, LH, and PO refers to the ratios of forest, farmland, water, low-density built-up, high-density built-up, extremely-high buildings, low buildings by grid, and population density, respectively.

This study further demonstrates that resident population density was a significant variable affecting the spatial variation of LST. This finding is in agreement with the results of several previous studies of the relationship between UHI and population density (Elvidge *et al.*, 1997; Oke, 1973). Since this study applied residential population density for the analysis, instead of actual population distribution, further studies of the LST/population distribution relationship are required.

The methodology has been developed specifically for Beijing, which has large census tracts. This methodology, however, provides an effective way to examine the relationship between LST and biophysical and demographic variables based on grid statistics. This procedure can overcome a major problem of the spatial aggregation approach, which uses census tracts or other census polygons as the statistical observation units. Thus, this methodology provides an alternative for urban studies, and may be applied to other cities in the world. Moreover, the findings of this study can be employed

TABLE 4. CO-LINEARITY DIAGNOSIS OF THE LINEAR REGRESSION EQUATION

			Variance Proportions								
Dimension	Eigenvalue	Condition Index	Constant	FO	FA	WA	LD	HD	EH	PO	LH
1	4.934	1.000	0.000	0.002	0.000	0.002	0.002	0.001	0.008	0.004	0.003
2	1.214	2.016	0.000	0.031	0.070	0.104	0.003	0.000	0.054	0.006	0.004
3	0.988	2.234	0.000	0.011	0.226	0.244	0.001	0.000	0.000	0.000	0.000
4	0.870	2.381	0.000	0.023	0.092	0.267	0.023	0.000	0.037	0.003	0.000
5	0.536	3.035	0.000	0.140	0.009	0.108	0.063	0.000	0.051	0.000	0.000
6	0.293	4.100	0.000	0.002	0.002	0.006	0.048	0.006	0.716	0.016	0.056
7	0.094	7.253	0.007	0.025	0.045	0.001	0.025	0.053	0.088	0.787	0.009
8	0.064	8.748	0.009	0.022	0.059	0.008	0.031	0.066	0.025	0.176	0.914
9	0.007	27.425	0.983	0.744	0.497	0.260	0.804	0.873	0.021	0.008	0.013

Note: FO, FA, WA, LD, HD, EH, LH, and PO refers to the ratios of forest, farmland, water, low-density built-up, high-density built-up, extremely-high buildings, low buildings, and population density by grid, respectively.

TABLE 5. RESULT OF PRINCIPAL COMPONENT ANALYSIS

				Variables							
Component	Eigenvalue	% of Variance	Cumulative %	FO	FA	WA	LD	HD	EH	PO	LH
Factor 1	3.452	43.155	43.155	−0.142	−0.084	−0.036	−0.119	0.261	0.214	0.257	0.258
Factor 2	1.352	16.903	60.058	0.419	0.073	0.470	−0.577	−0.016	0.062	0.028	−0.011
Factor 3	1.155	14.438	74.497	0.370	−0.796	0.099	0.254	−0.095	0.013	0.077	0.083
Factor 4	0.862	10.780	85.276	−0.532	−0.020	0.871	0.324	−0.075	−0.027	0.074	−0.004
Factor 5	0.582	7.278	92.555	0.145	0.209	−0.028	0.256	−0.508	1.093	0.184	−0.315
Factor 6	0.325	4.066	96.620	0.481	0.603	−0.002	0.418	−0.661	−0.530	0.995	0.773
Factor 7	0.199	2.486	99.106	0.113	0.194	0.127	0.170	−0.316	0.466	−1.442	1.592
Factor 8	0.072	0.894	100.000	1.677	1.093	0.615	1.815	2.469	0.262	−0.230	−0.289

Note: FO, FA, WA, LD, HD, EH, LH, and PO refers to the ratios of forest, farmland, water, low-density built-up, high-density built-up, extremely-high buildings, low buildings by grid, and population density, respectively.

to develop a theoretical basis for better urban planning policies to mitigate the UHI effects. For example, our results indicate that vegetation and water played a significant role in reducing the amount of thermal radiation. Therefore, it should be encouraged to enhance urban forest programs, and to consider outskirt farmlands and water bodies in the planning process. In contrast, high- and low-density built-up increased LST. To avoid serious UHI effects, local governments should take measures to damp heat islands by creating more greenbelts and canals. These planning implications are highly relevant if we consider that the 2008 Summer Olympic Games will be held in the city on August, the same month as the acquisition of our satellite images.

Acknowledgments

This research is supported by a Project of Knowledge Innovation of Chinese Academy of Sciences for research on the urban ecosystems in Beijing (KZCX2-YW-422) awarded to Dr. Zhiyun Ouyang. We would like to thank three anonymous reviewers for their constructive comments and suggestions.

References

Aniello, C., K. Morgan, A. Busbey, and L. Newland, 1995. Mapping micro-urban heat islands using Landsat TM and a GIS, *Computers & Geosciences*, 21:965–967.

Ben-Dor, E., and H. Saaroni, 1997. Airborne video thermal radiometry as a tool for monitoring miscroscale structures of the urban heat island, *International Journal of Remote Sensing*, 18:3039–3053.

Bornstein, R., and Q. Lin, 2000. Urban heat islands and summertime convective thunderstorms in Atlanta: Three case studies, *Atmospheric Environment*, 34:507–516.

Bottyán, Z., and J. Unger, 2003. A multiple linear statistical model for estimating the mean maximum urban heat island, *Theoretical and Applied Climatology*, 75:233–243.

Carson, T.N., R.R. Gillies, and E.M. Perry, 1994, A method to make use of thermal infrared temperature and NDVI measurements to infer surface soil water content and fractional vegetation cover, *Remote Sensing Review*, 9:161–173.

Carlson, T.N., and D.A. Ripley, 1997. On the relation between NDVI, fractional vegetation cover, and leaf area index, *Remote Sensing of Environment*, 62:241–252.

Cendese, A., and P. Monti, 2003. Interaction between an inland urban heat island and a sea-breeze flow: A laboratory study, *Journal of Applied Meteorology*, 42:1569–1583.

Chavez, P.S., 1996. Image-based atmospheric correction - Revisited and improved, *Photogrammetric Engineering & Remote Sensing*, 62(10):1025–1036.

Cheng, F., and K.H. Thiel, 1995. Delimiting the building heights in a city from the shadow in a panchromatic SPOT-image - Part 1: Test of forty-two buildings, *International Journal of Remote Sensing*, 16:409–415.

Chudnovsky, A., E. Ben-Dor, and H. Saaroni, 2004. Diurnal thermal behavior of selected urban objects using remote sensing measurements, *Energy and Buildings*, 36:1063–1074.

Dousset, B., and F. Gourmelon, 2003. Satellite multi-sensor data analysis of urban surface temperatures and landcover, *ISPRS Journal of Photogrammetry and Remote Sensing*, 58:43–54.

Eliasson, I., 1996. Urban nocturnal temperatures, street geometry and land use, *Atmospheric Environment*, 30:379–392.

Elvidge, C.D., K.E. Baugh, E.A. Kihn, H.W. Kroehl, E.R. Davis, and C.W. Davis, 1997. Relation between satellite observed visible-near infrared emissions, population, economic activity and

electric power consumption, *International Journal of Remote Sensing*, 18:1373–1379.

Fan, H., and D.J. Sailor, 2005. Modeling the impacts of anthropogenic heating on the urban climate of Philadelphia: A comparison of implementations in two PBL schemes, *Atmospheric Environment*, 39:73–84.

Flowerdew, R., and M. Green, 1989. Statistical methods for inference between incomparable zonal systems, *Accuracy of Spatial Databases* (M.F. Goodchild and S. Gopal, editors), Taylor and Francis, New York, pp. 239–248.

Gallo, K.P., and T.W. Owen, 1998, Assessment of urban heat island: a multi-sensor perspective for the Dallas-Ft. Worth, USA region, *Geocarto International*, 13:35–41.

Gillies, R.R., and T.N. Carlson, 1995, Thermal remote sensing of surface soil water content with partial vegetation cover for incorporation into climate models, *Journal of Applied Meteorology*, 34:745–756.

Gillies, R.R., T.N. Carlson, J. Cui, W.P. Kustas, and K.S. Humes, 1997, A verification of the 'triangle' method for obtaining surface soil water content and energy fluxes from remote measurements of the Normalized Difference Vegetation index (NDVI) and surface radiant temperature, *International Journal of Remote Sensing*, 18:3145–3166.

Goward, S.N., Y. Xue, and K.P. Czajkowski, 2002, Evaluating land surface moisture conditions from the remotely sensed temperature/vegetation index measurements: An exploration with the simplified simple biosphere model, *Remote Sensing of Environment*, 79:225–242.

Huang, H., R. Ooka, and S. Kato, 2005. Urban thermal environment measurements and numerical simulation for an actual complex urban area covering a large district heating and cooling system in summer, *Atmospheric Environment*, 39:6362–6375.

Liu, R.X., J. Kuang, Q. Gong, and X.L. Hou, 2003. Principal component regression analysis with SPSS, *Computer Methods and Programs in Biomedicine*, 71:141–147.

Lo, C.P., D. Quattrochi, and J. Luvall, 1997. Application of high-resolution thermal infrared remote sensing and GIS to assess the urban heat island effect, *International Journal of Remote Sensing*, 18:287–304.

Montgomery, D.C., and E.A. Peck, 1992. *Introduction to Linear Regression Analysis*, John Wiley & Sons, New York.

Moon, Z.K., and F.L. Farmer, 2001. Population density surface: A new approach to an old problem, *Society and Natural Resources*, 14:39–49.

Morris, C.J.G., I. Simmonds, and N. Plummer, 2001. Quantification of the influences of wind and cloud on the nocturnal urban heat island of a large city, *Journal of Applied Meteorology*, 40:169–182.

Oke, T.R., 1973. City size and the urban heat island, *Atmospheric Environment*, 7:769–779.

Oke, T.R., 1982. The energetic basis of the urban heat island, *Quarterly Journal of the Royal Meteorological Society*, 108:1–24.

Oke, T.R., R.A. Spronken-Smith, E. Jauregui, and C.S.B. Grimmond, 1999. The energy balance of central Mexico City during the dry season, *Atmospheric Environment*, 33:3919–3930.

Qin, Z., and A. Karnieli, 2001. A mono-window algorithm for retrieving land surface temperature from Landsat TM data and its application to the Israel-Egypt border region, *International Journal of Remote Sensing*, 22:3719–3746.

Saitoh, T.S., T. Shimada, and H. Hoshi, 1996. Modeling and simulation of the Tokyo urban heat island, *Atmospheric Environment*, 30:3431–3442.

Sobrino, J.A., J.C. Jimenez-Munoz, and L. Paolini, 2004. Land surface temperature retrieval from LANDSAT TM 5, *Remote Sensing of Environment*, 90:434–440.

Song, Y.L., and S.Y. Zhang, 2003. The study on heat island effect in Beijing during last 40 years, *Chinese Journal of Eco-Agriculture*, 11:126–129 (in Chinese).

Streutker, D.R., 2003. Satellite-measured growth of the urban heat island of Houston, Texas, *Remote Sensing of Environment*, 85:282–289.

Tong, H., A. Walton, J. Sang, and J.C.L. Chan, 2005. Numerical simulation of the urban boundary layer over the complex terrain of Hong Kong, *Atmospheric Environment*, 39:3549–3563.

Unger, J., 1999. Comparisons of urban and rural bioclimatological conditions in the case of a Central-European city, *International Journal of Biometeorology*, 43:139–144.

Voogt, J.A., and T.R. Oke, 1998. Effects of urban surface geometry on remotely-sensed surface temperature, *International Journal of Remote Sensing*, 19:895–920.

Weng, Q., 2001. A remote sensing-GIS evaluation of urban expansion and its impact on surface temperature in the Zhujiang Delta, China, *International Journal of Remote Sensing*, 22:1999–2014.

Weng, Q., 2003, Fractal analysis of satellite-detected urban heat island effect, *Photogrammetric Engineering & Remote Sensing*, 69(5):555–566.

Weng, Q., D. Lu, and J. Schubring, 2004, Estimation of land surface temperature-vegetation abundance relationship for urban heat island studies, *Remote Sensing of Environment*, 89:467–483.

Weng, Q., and S. Yang, 2004. Managing the adverse thermal effects of urban development in a densely populated Chinese city, *Journal of Environmental Management*, 70:145–156.

Yuan, Y., R.M. Smith, and W.F. Limp, 1997. Remodeling census population with spatial information from Landsat TM imagery, *Computers, Environment and Urban Systems*, 21:245–258.

(Received 12 May 2006; accepted 16 June 2006; revised 14 September 2006)